Many-body central force potentials for tungsten

Topical Review

Many-body central force potentials for tungsten

G Bonny[1], D Terentyev[1], A Bakaev[1,2,3], P Grigorev[1,4] and D Van Neck[2]

[1] SCK·CEN, Nuclear Materials Science Institute, Boeretang 200, B-2400 Mol, Belgium
[2] Center for Molecular Modeling, Department of Physics and Astronomy, Ghent University, Technologiepark 903, B-9052 Zwijnaarde, Belgium
[3] Faculty of Physics and Mechanics, Department of Experimental Nuclear Physics K-89, St. Petersburg State Polytechnical University, 29 Polytekhnicheskaya str., 195251 St. Petersburg, Russia
[4] FUSION-DC Department of Applied Physics, Ghent University, Sint-Pietersnieuwstraat 41 B4, B-9000 Gent, Belgium

E-mail: gbonny@sckcen.be

Abstract

Tungsten and tungsten-based alloys are the primary candidate materials for plasma facing components in fusion reactors. The exposure to high-energy radiation, however, severely degrades the performance and lifetime limits of the in-vessel components. In an effort to better understand the mechanisms driving the materials' degradation at the atomic level, large-scale atomistic simulations are performed to complement experimental investigations. At the core of such simulations lies the interatomic potential, on which all subsequent results hinge. In this work we review 19 central force many-body potentials and benchmark their performance against experiments and density functional theory (DFT) calculations. As basic features we consider the relative lattice stability, elastic constants and point-defect properties. In addition, we also investigate extended lattice defects, namely: free surfaces, symmetric tilt grain boundaries, the $1/2\langle 1\,1\,1\rangle\{1\,1\,0\}$ and $1/2\langle 1\,1\,1\rangle\{1\,1\,2\}$ stacking fault energy profiles and the $1/2\langle 1\,1\,1\rangle$ screw dislocation core. We also provide the Peierls stress for the $1/2\langle 1\,1\,1\rangle$ edge and screw dislocations as well as the glide path of the latter at zero Kelvin. The presented results serve as an initial guide and reference list for both the modelling of atomically-driven phenomena in bcc tungsten, and the further development of its potentials.

Keywords: tungsten, interatomic potential, dislocation

(Some figures may appear in colour only in the online journal)

1. Introduction

Tungsten (W) and tungsten-based alloys are the primary candidate materials for plasma facing components in fusion reactors. In the demonstration power plant (DEMO) and commercial reactors these materials will be exposed to unprecedented and unexplored irradiation conditions. The exposure to high-energy radiation (neutron damage, helium and hydrogen high temperature/flux plasma) severely damages the microstructure of the materials by violently displacing atoms from their lattice and thereby creating vacancy clusters, dislocation loops, voids and even microscopic bubbles. All the above mentioned radiation-induced processes cause profound macroscopic property changes that severely degrade the performance and lifetime limits of the in-vessel components [1].

In an effort to better understand the mechanisms driving the microstructure and embrittlement, material modelling is applied to complement experimental investigations [2, 3]. Among different modelling tools, large-scale atomistic simulations such as molecular dynamics (MD) are employed to investigate the mechanisms of plasticity [4–6] and primary damage creation [7–10]. At the core of such simulations lies the interatomic potential, which enables computation of the forces between interacting atoms. Currently, for tungsten more than 30 different interatomic potentials are available in the literature in the form of pair potentials [11–14], many-body central force potentials [15–31] and its empirical modification [32], bond order potentials [33–36], modified embedded atom method potentials [37–39] and fourth moment tight binding potentials [18, 40, 41]. Each potential comes with its strengths and weaknesses. Since all results hinge on the quality of the interatomic potential, it is important that its properties are well understood. Given the vast number of available potentials, a review summarizing their basic properties is in order.

In this work we focus on the many-body central force formalism, which offers a good compromise between transferability/predictability and computational speed, especially when it comes to large-scale finite-temperature simulations. The many-body central force framework was developed independently under the forms: 'embedded atom method' (EAM) [42], 'Finnis–Sinclair formalism [15]' and 'glue model [43, 44]'. We review the properties of 19 such potentials for W found in the literature [15–31]. As basic features we consider relative lattice stability, elastic constants and point-defect properties, which are all benchmarked against experimental data and density functional theory (DFT) calculations. In addition, we investigate extended lattice defects, namely: free surfaces, symmetric tilt grain boundaries, the $1/2\langle 1\,1\,1\rangle$ $\{1\,1\,0\}$ and $1/2\langle 1\,1\,1\rangle$ $\{1\,1\,2\}$ stacking fault energy profiles and the $1/2\langle 1\,1\,1\rangle$ screw dislocation (SD) core. We also provide the Peierls stress for $1/2\langle 1\,1\,1\rangle$ edge and SDs as well as the glide path of the latter at zero Kelvin.

2. Methods

A considerable amount of information on the properties of W is already available in the literature; however, we have used additional DFT calculations to extend the database for several defects not yet described in the open literature.

The DFT calculations were performed using the Vienna ab initio simulation package (VASP) [45, 46]. VASP is a plane-wave DFT code that implements the projector augmented wave (PAW) method [47, 48]. Standard PAW potentials supplied with VASP were used with the Vosko–Wilk–Nusair parameterization [49] for the local density approximation (LDA) combined with the Perdew–Wang [50] parameterization for the generalized gradient approximation (GGA) correction. A potential with six valence electrons was used and the plane wave cut-off was set to 450 eV. Brillouin zone sampling was performed using the

Table 1. Details of the calculation set-up for the different DFT and EAM calculations.

Configuration	DFT				EAM		
	Periodicity	N_{atoms}	Size (a_0^3)	k-points	Periodicity	N_{atoms}	Size (a_0^3)
Bulk	3D	128	$4.0 \times 4.0 \times 4.0$	$7 \times 7 \times 7$	3D	2000	$10.0 \times 10.0 \times 10.0$
Free surface	2D				2D		
$\{1\,0\,0\}$		252	$3.0 \times 3.0 \times 18.7$	$5 \times 5 \times 1$		2000	$10.0 \times 10.0 \times 10.0$
$\{1\,1\,0\}$		144	$21.7 \times 2.4 \times 1.7$	$1 \times 7 \times 9$		2016	$9.9 \times 9.8 \times 10.4$
$\{1\,1\,1\}$		288	$4.2 \times 4.9 \times 11.6$	$3 \times 1 \times 1$		2016	$9.9 \times 9.8 \times 10.4$
$\{1\,1\,2\}$		144	$2.8 \times 14.5 \times 2.6$	$5 \times 1 \times 6$		2016	$9.9 \times 9.8 \times 10.4$
γ-surface cut	2D				2D		
$1/2\langle 1\,1\,1\rangle\,\{1\,1\,0\}$		60	$18.9 \times 2.4 \times 0.9$	$1 \times 7 \times 11$		6300	$21.2 \times 12.2 \times 12.1$
$1/2\langle 1\,1\,1\rangle\,\{1\,1\,2\}$		90	$1.4 \times 41.5 \times 0.99$	$9 \times 1 \times 9$		3780	$12.7 \times 12.2 \times 12.1$
Grain boundary	3D				2D		
$\Sigma 3\langle 1\,1\,0\rangle\,\{1\,1\,1\}$		72	$1.4 \times 2.4 \times 10.6$	$9 \times 5 \times 1$		2304	$5.6 \times 7.3 \times 27.8$
$\Sigma 3\langle 1\,1\,0\rangle\,\{1\,1\,2\}$		96	$2.8 \times 1.7 \times 9.9$	$7 \times 9 \times 1$		1632	$5.6 \times 5.2 \times 28.0$
$\Sigma 5\langle 1\,0\,0\rangle\,\{0\,1\,3\}$		120	$1.0 \times 3.2 \times 19.2$	$9 \times 5 \times 1$		3120	$9.0 \times 12.6 \times 22.1$
$\Sigma 11\langle 1\,1\,0\rangle\{1\,1\,3\}$		112	$1.4 \times 6.6 \times 6.1$	$9 \times 1 \times 1$		4032	$5.6 \times 9.9 \times 28.0$
$\Sigma 9\langle 1\,1\,0\rangle\{1\,1\,4\}$		192	$1.4 \times 8.5 \times 8.2$	$9 \times 1 \times 1$		3600	$5.6 \times 12.7 \times 28.1$
$\Sigma 9\langle 1\,1\,0\rangle\{2\,2\,1\}$		160	$1.4 \times 6.0 \times 9.7$	$9 \times 1 \times 1$		2856	$5.6 \times 9.0 \times 28.2$
$\Sigma 19\langle 1\,1\,0\rangle\,\{3\,3\,1\}$		308	$1.4 \times 8.7 \times 12.7$	$9 \times 1 \times 1$		5040	$5.6 \times 13.0 \times 28.2$
$\langle 1\,1\,1\rangle$ atomic row displacement	3D	36	$4.2 \times 4.9 \times 0.9$	$3 \times 2 \times 9$	3D	2160	$14.1 \times 14.7 \times 5.2$
Dislocation	1D				2D		
$1/2\langle 1\,1\,1\rangle$ screw		108	$10.0 \times 8.8 \times 0.9$	$1 \times 1 \times 12$		18144	$49.5 \times 49.0 \times 5.2$
$1/2\langle 1\,1\,1\rangle$ edge		NA	NA	NA		22662	$49.5 \times 7.3 \times 86.6$

Monkhorst–Pack scheme, where the k-point meshes differ depending on the box size and are given in table 1. Finite-temperature smearing was obtained following the Methfessel–Paxton method with a smearing width of 0.3 eV. The ionic relaxation was performed using the conjugate gradient optimization scheme with a force convergence criterion of 0.03 eV Å^{-1}.

The EAM calculations were performed using a standard MD code. The ionic relaxation was performed using the conjugate gradient optimization scheme, a quenching relaxation scheme or a combination of both, with an accuracy of 1 meV on the total energy.

The specifics of box size and boundary conditions depend on the calculated property and are summarized in table 1. The bulk properties and $\{1\,0\,0\}$ free surface energy were calculated using a simulation box with principal axes oriented along the [1 0 0], [0 1 0] and [0 0 1] directions. For all other properties the principal axes of the simulation box were oriented along the [1 1 0], [$\bar{1}$ 1 2] and [1 $\bar{1}$ 1] direction, except for grain boundary (GB) calculations, which all have different orientations of the axes depending on the GB type (see below).

In the present work all values for the binding energy of a configuration containing the objects X_i is defined as,

$$E_{\text{b}}\left(X_1 \ldots X_n\right) = \sum_i E(X_i) - \left[E\left(\sum_i X_i\right) + (n-1)\,E_{\text{ref}} \right], \tag{1}$$

where E_{ref} is the energy of the super cell without any objects (bcc W), $E(X_i)$ is the energy of the supercell containing the single object X_i, and $E\left(\sum_i X_i\right)$ is the energy of the super cell containing all interacting objects. Within this definition positive values of E_{b} denote attraction.

The surface energy for a (klm) free surface, $\gamma_{(klm)}$, is given as,

$$\gamma_{(klm)} = \frac{E_{(klm)} - N_{\text{atoms}}\, E_{\text{coh}}}{2\,S}, \tag{2}$$

with $E_{(klm)}$ the total energy of the crystal with free surfaces, N_{atoms} the number of atoms in the box, E_{coh} the cohesive energy of the perfect crystal, and S the area of the free surface.

The stacking fault energy, γ_{SF}, in the γ-line profiles was calculated as,

$$\gamma_{\text{SF}} = \frac{E_{\text{SF}} - N_{\text{atoms}}\, E_{\text{coh}}}{S} - 2\,\gamma_{\text{FS}}, \tag{3}$$

with E_{SF} the total energy of the crystal with stacking fault and γ_{SF} the free surface energy as calculated from equation (2).

The investigated GBs were prepared considering mirror symmetry for bi-crystals. The principal axes of the crystals x, y and z correspond to the tilt axis, GB axis and normal to GB plane, respectively. The initial separation between two layers belonging to different grains was set as equal to that inside the grains. In the DFT calculations 3 D periodic super cells were used and the GB energy, γ_{GB}, was calculated following equation (2), where $E_{(klm)}$ was replaced by the total energy of the crystal containing the GB. In the EAM calculations 2D periodic super cells along the x and y directions were used. Free surfaces were applied perpendicular to the GB plane so the optimal spacing between the two grains was achieved automatically during the relaxation procedure. In this case, γ_{GB} was calculated following equation (3), where E_{SF} was replaced by the total energy of the crystal containing the GB.

For the study of dislocation properties, the principal axes x, y and z of the bcc crystal were oriented along the [1 1 0], [$\bar{1}$ 1 2] and [1 $\bar{1}$ 1] directions, respectively. All studies were performed using ionic relaxation at zero Kelvin. The dislocation core structure was analysed using Vitek differential displacement maps [51]. In the DFT calculations a cylindrical crystal with periodic boundary condition along the dislocation line (created along the cylinder axis) was applied. The 40 atoms forming the outer surface of the cylinder were fixed to avoid the restoration to the perfect crystal upon relaxation. In the EAM calculations we employed the simulation model developed by Osetsky and Bacon [52]. The initial straight edge dislocation (ED) or SD with yz slip plane was created along the y or z direction with the Burgers vector $\boldsymbol{b} = 1/2[1\,1\,1]$ parallel to z. Standard periodic boundary conditions were applied along the y and z directions for the ED, while modified periodic conditions (with $b/2$ shift along the y direction, as proposed by Rodney [53]) were applied for the SD. The simulation box was divided into three parts along x. The upper and lower parts consist of several atomic planes in which atoms were rigidly fixed in their original positions, whereas atoms in the 'inner' region were free to move during the ionic relaxation cycles. A glide force on the dislocation was generated by the relative displacement of the rigid blocks in the z direction, corresponding to a simple shear strain, ε_{xz}. The corresponding resolved shear stress induced by the applied deformation was calculated as $\tau = F_z/S_{yz}$, where F_z is the total force in the z direction on the lower outer block resulting from all atoms in the inner region, and S_{yz} is the area of the yz cross section of the box. The force, F_z, was computed after relaxation of the crystal so that the maximum force acting on any 'inner' atom in the system did not exceed $1\,\text{meV}\,\text{Å}^{-1}$. It was verified that the chosen parameterisation, i.e., box size and relaxation criterion, provides full convergence of the results with a tolerance in the Peierls stress of $\sim 2\,\text{MPa}$. In addition to the numerical output, we have visualized the evolution of the dislocation core position and structure, using a combination of common neighbour analysis and potential energy [53].

Table 2. Nomenclature and remarks on the investigated many-body central force potentials.

Abbreviation	Reference	Remark
FS	Finnis and Sinclair, 1984 [15]	
AT	Ackland and Thetford, 1987 [16]	Minor upgrade in short range part FS
JO	Johnson and Oh, 1989 [17]	
FOI	Foiles, 1993 [18]	
WB	Wang and Boercker, 1995 [19]	Fcc more stable than bcc
ZWJ	Zhou *et al* 2001 [20]	
KLL	Kong *et al* 2002 [21]	
GKL	Gong *et al* 2003 [22]	Fcc more stable than bcc
ZSG	Zhang *et al* 2004 [23]	
ZKG	Zhang *et al* 2004 [24]	Identical to ZSG except for 0.02 Å in cut-off range
ZSY	Zhang *et al* 2005 [25]	Fcc more stable than bcc
DLK	Dai *et al* 2007 [26]	
DND	Derlet *et al* 2007 [27]	
BND	Björkas *et al* 2009 [28]	Stiffened version of DND
JW	Juslin and Wirth, 2013 [29]	Minor upgrade in short range part AT and stiffening
MVG1	'EAM-2' of Marinica *et al* 2013 [30]	
MVG2	'EAM-3' of Marinica *et al* 2013 [30]	
MVG3	'EAM-4' of Marinica *et al* 2013 [30]	
WZL	Wang *et al* 2014 [31]	

The latter allowed us to establish the mechanism of dislocation movement and to identify the glide plane under [1 1 1] (1$\bar{1}$0) pure shear load.

3. Literature study

In this section we describe all many-body central force type potentials that are considered in the present work. We also correct some typographical errors found in the respective papers and report upon properties that we could not reproduce. For convenience, an overview of nomenclature of all considered potentials is given in table 2.

The first potential considered here is the one developed by Finnis and Sinclair (FS) [15] in 1984. The latter work in fact concerns the development of a new many-body central force potential formalism, namely, the so called 'Finnis–Sinclair' formalism. As an application, potentials for the bcc transition metals were fitted to the experimental lattice parameter, cohesive energy, elastic constants and vacancy formation energy.

In 1987 the same potential was modified in the short range region by Ackland and Thetford (AT) [16] to predict a more realistic pressure–volume relationship. Given the small changes induced by this modification, all properties obtained for FS are also valid for AT, unless explicitly stated otherwise.

In 1989 Johnson and Oh (JO) [17] developed an analytical parameterization and fitting methodology within the EAM for bcc transition metals. The potentials were fitted to the same experimental properties as FS. We note that although we find the reported

lattice parameter and cohesive energy, we could not reproduce the elastic constants (see table 3).

In 1993 Foiles (FOI) [18] developed 'fourth moment' Finnis–Sinclair type potentials and EAM ones for W and Mo. The latter were developed as a benchmark for the fourth moment ones. The EAM potentials were fitted to the same experimental properties as FS. In his paper we found a typographical error in the cut-off function that should read: $x^3(6x - 15x + 10)$. In addition, the cut-off distance was not defined for the pair potential, which we chose to be 3.5 Å. The latter distance is close to the zero cross-over of the pair potential function. As a peculiarity of the potential, we remark that at zero density the embedding function has a value of -5.16 eV, whereas this value is generally 0 eV.

In 1995 Wang and Borcker (WB) [19] provided EAM-like parameterizations for bcc transition metals with an emphasis on the reproduction of experimental phonon spectra. This was realized by the introduction of Friedel oscillations in the density function. To avoid the possibility of a negative density due to those oscillations, the total density is biased by an additive constant and therefore the latter is formally not of EAM-type. Nevertheless, we tested the reported parameterization and could reproduce the reported lattice parameter ($a_0 = 3.16259$ Å) and cohesive energy ($E_c = 8.6588$ eV) for the bcc lattice. However, we found the fcc lattice with lattice parameter ($a_0 = 4.06877$ Å) and cohesive energy ($E_c = 8.7276$ eV) to be more stable, in contrast to the claims in the paper. Therefore the latter potential was not considered any further in the present review.

In 2001 Zhou *et al* (ZWJ) [20] developed a set of interatomic potentials for 16 transition metals and their binary alloys. The potentials for the pure elements were fitted to the same properties as FS and the alloys were fitted to the heats of solution. Although the provided parameterizations are complete, we could not retrieve any references with respect to the target data used to fit the potentials.

In 2002 Kong *et al* (KLL) [21] developed a potential for the WCu system to study bcc/fcc interfacial reactions. The potential for W was fitted to the same experimental properties as FS. We remark on a typographical error in the reference to the experimental work reported in table I of the paper: reference "[14]" should read "[9]" instead. The latter reference refers to the work of Finnis and Sinclair [15], but we note that for the vacancy formation energy the calculated value from table 2 of the latter work was used as a fitting target instead of the experimental value. Finally, we note that although we can reproduce the reported lattice constant and cohesive energy, the elastic constants cannot be reproduced (see table 3).

In 2003 Gong *et al* (GKL) [22] also developed a potential for the WCu system to study glass formation. In the paper we found a typographical error in formula (7), which must read: $k_a = 4.5\{1 + 4/[\frac{2C_{44}}{(C_{11} - C_{12})} - 0.1]\}$. We tested the corrected parameterization and could reproduce all reported values, i.e., lattice constant ($a_0 = 3.16475$ Å), cohesive energy ($E_c = 8.6600$ eV) and elastic constants ($C_{11} = 533$ GPa, $C_{12} = 205$ GPa and $C_{44} = 163$ GPa). However, we found the fcc lattice with lattice parameter ($a_0 = 4.07815$ Å) and cohesive energy ($E_c = 8.6719$ eV) to be more stable than the bcc one. Therefore the latter potential was not considered any further in the present review.

In 2004 two binary potentials were developed by Zhang *et al* [23, 24]. The first one (ZSG) [23] was developed in the framework of the study of metastable phases in the AgW system. The second one (ZKG) [24] focussed on glass formation in the CuW system. Both W potentials were fitted to the same experimental properties as FS and only differ by 0.02 Å in the cut-off distance. Despite this small difference, both potentials lead to equivalent results. Therefore all results reported for ZSG are also valid for ZKG unless explicitly stated. We remark that we could not retrieve the reported target values for cohesive and vacancy formation

Table 3. Comparison between experiments, DFT and potentials with respect to the lattice parameter and cohesive energy of close packed lattices, elastic constants, formation energy of different self-interstitial configurations, vacancy formation and migration energy and binding energy of di-vacancies. The target data to which the potentials were fitted are indicated by footnotes a...i.

Property	Exp.	DFT	FS	JO	FOI	ZWJ	KLL	ZSG	DLK	DND	MVG1	MVG2	MVG3	WZL
a_0 (bcc) (Å)	3.1652[a,d,f,i] [54, 68, 69] 3.16475[b,c] [70] 3.1648[h] [71]	3.19 [67] 3.172 [72] 3.14 [73] 3.178[j]	3.16520	3.16475	3.16347	3.16519	3.16500	3.16500	3.18356	3.16520	3.14000	3.18738	3.14339	3.16519
a_0 (fcc) (Å)		4.054[h] [67] 4.025 [72] 4.029[j]	3.92700	4.11944	4.1193	4.12194	4.05534	4.11222	3.77264	3.98946	4.05340/ 3.79258	4.19954/ 3.82918	4.05339/ 3.79588	3.97810
E_c (bcc) (eV)	8.90[a,d,f,i] [54, 71] 8.66[b,c] [57] 9.89 [68]	8.48 [72] 9.97 [73]	8.9000	8.6600	8.8598	8.7590	8.9000	8.6600	8.4003	8.9000	8.9000	8.8992	8.9000	8.8999
E_c (fcc) (eV)		8.43[h,m] [67] 8.37[m] [74] 8.42[m] [26] 8.41[m] [72]	8.7454	8.6045	8.8557	8.5969	8.8069	8.6067	7.9088	8.8476	8.4300/ 8.5272	8.4456/ 8.5362	8.4300/ 8.5161	8.8080
E_c (hcp) (eV)		8.34[n] [26]	8.7454	8.6045	8.8557	8.5969	8.8069	8.6067	7.8601	8.8476	8.5624	8.5445	8.5605	8.8080
C_{11} (GPa)	522[a,b,c,d,f] [56, 75] 533[l] [54] 523[h,k] [54, 71, 76] 529 [77] 521[i] [78]	488 [67] 517 [66] 526 [79] 515 [64]	523	503	543	524	679	533	531	524	523	474	523	523
C_{12} (GPa)	204[b,c] [56, 75] 205[a,d,f,k,l] [54, 76] 203[h] [71] 209 [77] 202[i] [78]	200 [67] 203 [66] 194 [79] 197 [64]	205	185	215	205	361	205	188	205	203	192	202	205
C_{44} (GPa)	161[a,b,c,d,f,k] [54, 56, 75, 76] 163[l] [54] 160[h,i] [71, 78] 162 [77]	137 [67] 161 [66] 146 [64, 79]	161	161	163	161	161	163	147	161	160	148	161	161
$E_f \langle 1\,1\,1 \rangle$ (eV)		9.55[f,g,i] [80] 10.53[h] [67] 10.44 [67] 9.82 [81] 10.09 [79] 9.73[j]	8.87°, 9.52[p], 7.81	8.05	8.48	10.55	16.21	12.22	9.32	9.48	10.40	10.15	10.40	9.48
$E_f \langle 1\,1\,0 \rangle$ (eV)		9.84[f,g,i] [80] 10.82[h] [67] 10.79 [67] 10.10 [81] 10.55 [79] 10.04[j]	9.62°, 10.19[p], 8.45	7.77	7.95	9.70	16.22	10.78	8.53	9.78	10.86	10.99	10.89	9.81
$E_f \langle 1\,0\,0 \rangle$ (eV)		11.49[f,g,i] [80] 12.87 h [67] 11.74 [81] 12.20 [79] 11.74[j]	9.80°, 10.30[p], 8.66	9.35	9.58	12.20	16.00	14.85	9.05	11.34	12.93	11.32	12.81	11.41
E_f (Octa) (eV)		11.68[f,g] [80] 13.11[h] [67]	9.98°, 10.41[p], 8.87	9.46	10.71	12.02	20.95	14.90	9.04	11.57	12.73	11.11	12.62	11.59

Table 3. (Continued.)

Property	Exp.	DFT	FS	JO	FOI	ZWJ	KLL	ZSG	DLK	DND	MVG1	MVG2	MVG3	WZL
E_f (Tetra) (eV)		11.05[f,g,i] [80] 12.47[h] [67]	9.97[o], 10.47[p], 8.82	8.78	9.22	11.52	14.28	13.77	9.12	10.92	12.01	11.39	11.95	10.86
E_f (Vac) (eV)	3.15[a,d] [82] 3.95[b,c] [58–60] 3.5 [71] 4.1 [71] 3.67 ± 0.2 [83] 4.0 ± 0.3 [58] 3.76 ± 0.39 [84]	3.56[f,g,i] [80] 3.49[h] [67] 3.25 [67] 3.23 [67] 3.54 [67] 3.20 [21] 3.34 [85] 3.06[j]	3.63, 3.71[p]	3.55	3.28	3.58	3.42	3.57	3.48	3.56	3.49	4.36	3.82	3.57
E_m (Vac) (eV)	1.7 [71] 2.0 [71] 1.78 ± 0.1 [83]	1.78 [67,80] 1.66 [81] 1.71 [85] 1.65 [21] 1.68[j]	1.45	1.95	2.25	1.90	1.97	2.29	1.77	2.07	1.85	0.99	1.84	1.43
E_b(V-V) 1nn (eV)	0.7 [86]	0.41 [27] 0.01 [79] 0.03 [79] −0.09 [67] −0.03 [67] −0.04 [67] −0.06 [81] 0.05 [87] −0.18[j]	0.43, 0.47[p]	0.31	0.27	0.37	0.36	0.31	0.37	0.57	0.49	0.46	0.52	0.44
E_b (V-V) 2nn (eV)		0.19 [27] −0.19 [79] −0.37 [79] −0.41 [67] −0.47 [67] −0.44 [67] −0.40 [81] −0.27 [87] −0.49[j]	0.40, 0.41[p]	0.47	0.43	0.46	0.38	0.45	0.37	0.37	0.38	0.61	0.45	0.39

[a] Target data FS.
[b] Target data JO.
[c] Target data FOI.
[d] Target data KLL.
[e] Target data ZSG.
[f] Target data DND.
[g] Target data JW.
[h] Target data MVG1, MVG2 and MVG3.
[i] Target data WZL.
[j] DFT data obtained in this work.
[k] Data obtained at 300 K [54].
[l] Extrapolated data to 0 K [54].
[m] Experimental value for bcc (8.90 eV) augmented by the DFT calculated energy difference between fcc and bcc.
[n] Experimental value for bcc (8.90 eV) augmented by the DFT calculated energy difference between hcp and bcc.
[o] AT.
[p] JW.

energy from the quoted references, which are [54–56]. Instead, the reported target values are consistent with [57] and [58–60] for the cohesive energy and vacancy formation energy, respectively.

In 2005 Zhang *et al* (ZSY) [25] developed a potential for the ScW system to study the formation of amorphous alloys by ion beam mixing. We could not reproduce the reported

cohesive energy for the bcc lattice ($E_c = 8.42$ eV compared to a reported $E_c = 8.66$ eV). The optimum lattice parameter and elastic constants for the bcc lattice, on the other hand, could be reproduced. Moreover, we found that the fcc lattice with lattice parameter ($a_0 = 4.08256$ Å) and cohesive energy ($E_c = 8.4432$ eV) is more stable than the bcc one. Therefore the latter potential was not considered any further in the present review.

In 2007, independently of each other, two potentials were developed. Dai *et al* (DLK) [26] developed long-range Finnis–Sinclair type potentials for bcc transition metals to improve the prediction of the relative stability between competing close packed lattices. The potentials were fitted to the same experimental properties as FS. Derlet *et al* (DND) [27] developed potentials for bcc transition metals in the framework of a DFT and classical MD study with respect to the migration of interstitials. The potentials were fitted to the experimental lattice parameter, cohesive energy and elastic constants. In addition, it was fitted to the DFT calculated formation energy of the mono-vacancy and several self-interstitial configurations.

In 2009 the latter potential (and the one for molybdenum) (DND) was stiffened to the Ziegler–Biersack–Littmark (ZBL) [61] function by Björkas *et al* (BND) [28] to simulate collision cascades in W (and Mo). The stiffening does not affect the equilibrium properties of DND and therefore all obtained results for DND are also valid for BND, unless explicitly stated.

In 2013 AT was further modified and stiffened by Juslin and Wirth (JW) [29] to study He bubble formation in W. Besides the stiffening to the ZBL potential, the AT short range part was modified to better fit the DFT calculated formation energy of self-interstitial configurations. As most of the equilibrium properties remain unchanged compared to FS (and therefore also AT), all properties obtained for FS are also valid for JW, unless explicitly stated.

In the same year, 2013, three potentials were developed by Marinica *et al* (MVG1, MVG2 and MVG3) [30] to model radiation defects and dislocations in W. The potentials themselves represent refits of DND and are fitted to the same DFT data on lattice defects (as used for DND), as well as to new DFT calculated forces from liquid state configurations (see for example [62, 63]). In addition, the potentials were forced to provide a non-degenerate core structure for a $1/2\langle 1\,1\,1\rangle$ SD, as predicted by DFT [64–66]. We remark a typographical error in table 1 of paper [30], where reference [42] must be replaced by [67] in the present paper. We note that for MVG1 and MVG2 the reported elastic constants could not be reproduced (see table 3).

In 2014 an additional potential was developed by Wang *et al* (WZL) [31]. The potential is based on DFT calculations and focusses on self-interstitial defects and the thermal expansion of W. We note a typographical error in table 2 of the paper: the parameters with and without primes are switched.

4. Lattice stability, point-defects and elastic constants

In table 3 the lattice stability, elastic constants, interstitial and vacancy formation energy, vacancy migration and di-vacancy binding energy calculated by the above selected potentials is presented. In the same table, the obtained values are compared to DFT and experimental data (target data to which the potentials were fitted are indicated by [a] ...[i]).

Focusing on the lattice stability first, all potentials were fitted to the experimental or DFT-obtained bcc lattice constants and cohesive energy, in particular, FS, KLL and DND were fitted to [54], JO, FOI and ZSG to [57, 70], MVG1, MVG2 and MVG3 to [71], and WZL to [54, 69]. For ZWJ and DLK, however, no references regarding the target data were given. In addition to the bcc data, MVG1, MVG2 and MVG3 were also fitted to the DFT-obtained fcc lattice constant
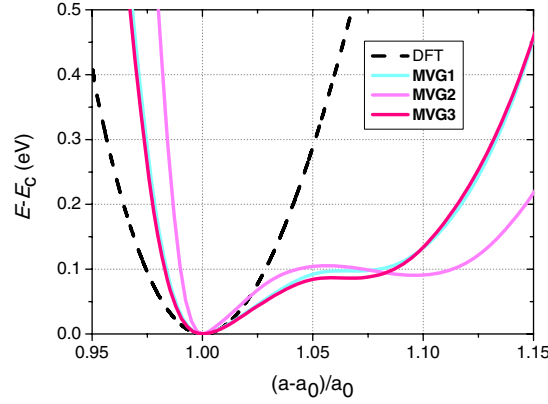
Figure 1. The cohesive energy difference for the fcc lattice as a function of relative lattice parameter variation calculated by both DFT and potentials.

and cohesive energy [30, 67]. We observe that all potentials and DFT data are in excellent or satisfactory (<10% deviation) agreement with the experimental bcc lattice constant and cohesive energy. Furthermore, for all potentials the bcc lattice is the ground state, compared to other close packed structures such as fcc (Strukturbericht A1) and hcp (Strukturbericht A3). We remark that the lattice constant and cohesive energy for the fcc lattice reported in [30] for MVG1, MVG2 and MVG3 corresponds to a local minimum in the energy landscape, with the global minimum about 0.1 eV lower. As shown in figure 1, the latter is an artefact of the potentials as DFT data shows a single minimum for the fcc lattice. We note that only the latter potentials exhibit this peculiarity.

With respect to the elastic constants, all potentials were fitted to experimental data, in particular, FS, KLL and DND were fitted to [75], JO, FOI and ZSG to [56], MVG1, MVG2 and MVG3 to [71], and WZL to [78]. Note that for ZWJ and DLK no references for the target data were provided. All potentials and DFT data, except for KLL, are in excellent or satisfactory (<10% deviation) agreement with the experimental data. For KLL the deviations for C_{11} and C_{12} reach 70%, while all reported DFT data are within 10% of the experimental results.

Regarding the formation energy of self-interstitial configurations, all reported DFT data suggest the $\langle 1\,1\,1 \rangle$ crowdion as the most stable configuration. This is respected by FS, AT, DND, JW, MVG1, MVG2, MVG3 and WZL, while JO, FOI, ZWJ, ZSG and DLK predict the $\langle 1\,1\,0 \rangle$ dumbbell and KLL the $\langle 1\,0\,0 \rangle$ dumbbell as the most stable self-interstitial configuration. We remark that only DND, JW, MVG1, MVG2, MVG3 and WZL were explicitly fitted to ensure the appropriate order in the formation energy of the interstitial configurations, namely, DND, JW and WZL to DFT data from [80] and MVG1, MVG2 and MVG3 to DFT data from [67].

All potentials were also fitted to the experimental or DFT calculated vacancy formation energy. In particular, FS and KLL were fitted to [82], JO, FOI and ZSG to [58–60], DND and WZL to [80], and MVG1, MVG2 and MVG3 to [67]. We note, that for ZWJ and DLK no references regarding the target data were given. All potentials and DFT data are in good agreement with experiments, providing results within the experimental range, i.e., 3.15–4.1 eV.

The vacancy migration barrier was not explicitly fitted for any of the potentials. Nevertheless, all the potentials and DFT data, except for FS, FOI, ZSG, MVG2 and WZL, are within 10% of the experimental range (1.7–2.0 eV). Besides the absolute value, the migration barrier curvature followed by a migrating atom exchanging its position with a vacancy is also
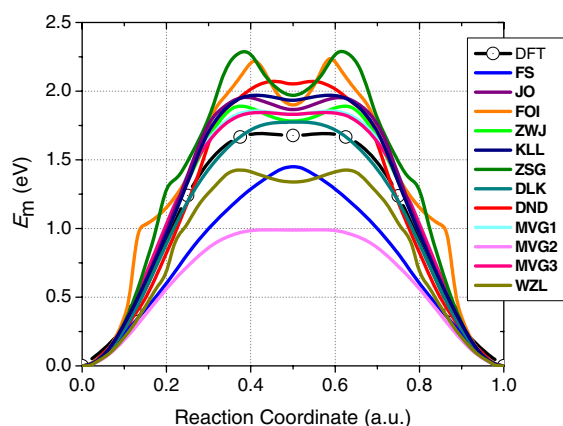
Figure 2. The vacancy migration energy path calculated by both DFT and the potentials.

of importance. In figure 2 we compare the vacancy migration energy path between DFT and the potentials. The DFT curve shows a plateau (or shallow minimum) around the saddle point. This specific shape is reproduced by JO, ZWJ, KLL, DND, MVG1, MVG2, MVG3 and WZL. However, more important than this specific shape is the overall smoothness of the curve. We note that in addition to the latter, FS and DLK exhibit a smooth curve, while FOI and ZSG reveal unphysical humps.

With respect to the binding energy of the di-vacancy, the combined field-ion microscopy and electrical resistivity experiments by Park *et al* [86] predict a strong binding (0.7 eV) and suggest that the first nn configuration is the ground state for the di-vacancy. While all DFT data indicate lower binding or stronger repulsion for the second nn di-vacancy complex compared to the first nn configuration, only the study by Derlet *et al* [27] reports significant binding (0.41 eV) for the first nn configuration. All other data suggests insignificant binding or repulsion. The origin of the vacancy–vacancy repulsion in the second nn configuration is explained in [30] in terms of the shape of the distribution of the local density of states near the Fermi level obtained by DFT calculations. The latter is a purely quantum mechanical effect that is not expected to be reproducible by empirical many-body central-force potentials. Indeed, DND, JW, MVG1 and MVG3 predict the first nn configuration of the di-vacancy to be significantly more stable than the second nn one. All other potentials, except for FS, AT, DLK and WZL that provide similar binding for the two configurations, underestimate the experimental binding energy.

5. Extended defects

5.1. Surface defects

In figure 3 we present the relative energy difference of several low index free surfaces, namely: {1 0 0}, {1 1 1} and {1 1 2}, taking {1 1 0} as baseline, which has the lowest formation energy. The presented DFT data sets give similar results, except for the {1 1 1} free surface that shows a discrepancy of about 200 mJ m^{-2}. As shown in the figure, all potentials predict the {1 1 0} surface to be the most stable, consistent with DFT. With respect to the DFT trends, only DND consistently predicts the highest formation energy for the {1 0 0} surface orientation. In fact, the resulting curve from DND is also in good quantitative agreement with the DFT
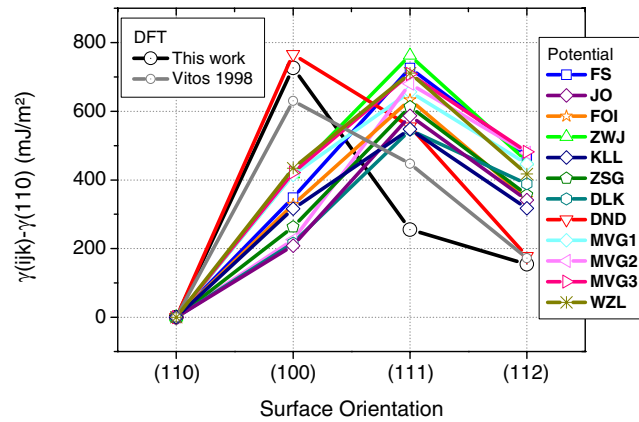
Figure 3. Free surface energy per unit area for various low index surface configurations.

Table 4. Reference value for the (1 1 0) free surface energy obtained from experiment, DFT calculations and the potentials.

Property	Exp.	DFT	FS	JO	FOI	ZWJ	KLL	ZSG	DLK	DND	MVG1	MVG2	MVG3	WZL
$\gamma_{(1\,1\,0)}$ (mJ m^2)	3250 [89]	3197^a	2575	2600	2440	2566	2435	2629	2649	2402	2306	3096	2509	2402
	3675 [90]	4005 [88]												

^{a} DFT data obtained in this work.

data from [88]. Other potentials predict that the {1 1 1} surface requires the highest formation energy. In table 4 we report the absolute values for the {1 1 0} surface as calculated by the potentials and DFT [88], as well as the experimental data [89, 90]. While the DFT values and results for MVG3 are within 10% of the experimental data range, the other potentials remarkably underestimate the formation energy of the {1 1 0} surface.

In figures 4 and 5 we present the stacking fault energy for $1/2\langle 1\,1\,1\rangle$ {1 1 0} and $1/2\langle 1\,1\,1\rangle$ {1 1 2} shear, respectively, calculated by both DFT [91] and the potentials. The stacking fault energy profiles (henceforth referred to as γ-line) provide information about the energy landscape for the shear process of a perfect crystal in {1 1 0} and {1 1 2} atomic planes, and can be used to compute the dislocation core structure and Peierls stress [92, 93]. As shown in the figures, all DFT data predicts smooth curves with a single well-defined maximum. On the γ-lines obtained using FOI, ZSG and DND we identify unphysical humps, while other potentials provide a curvature in agreement with the DFT result. The saddle point in the γ-lines predicted by JO, KLL, ZWJ, MVG1 and MVG3 is within 10% of the DFT data, in the case of the $1/2\langle 1\,1\,1\rangle$ {1 1 0} shear. In the {1 1 2} plane, a good quantitative prediction (i.e. within 10%) is achieved only by MVG1 and MVG3.

Comparison of the GB energies is presented in figure 6. All the potentials accurately predict the energy of the $\Sigma3\langle 1\,1\,1\rangle$ {1 1 2} tilt boundary as compared to the DFT data. The deviation from the DFT results is especially significant in the case of GBs with $\langle 1\,1\,0\rangle$ tilt axis. Indeed, these GBs reveal essential reconstruction of the atoms at the interface, which apparently cannot be easily reproduced by the potentials. Regarding quantitative accuracy, none of the potentials is capable of predicting the interface energy within 10% of all the DFT data. FOI and ZSG reveal the strongest deviation from the DFT prediction. The appropriate
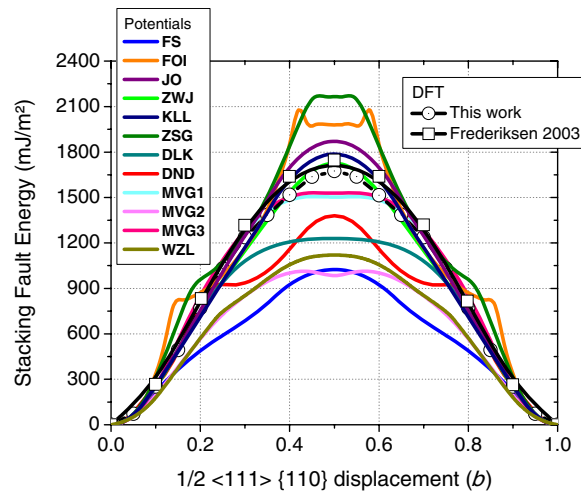
Figure 4. Comparison between DFT and the potentials of the $1/2\langle 1\,1\,1\rangle\{1\,1\,0\}$ stacking fault energy profile.
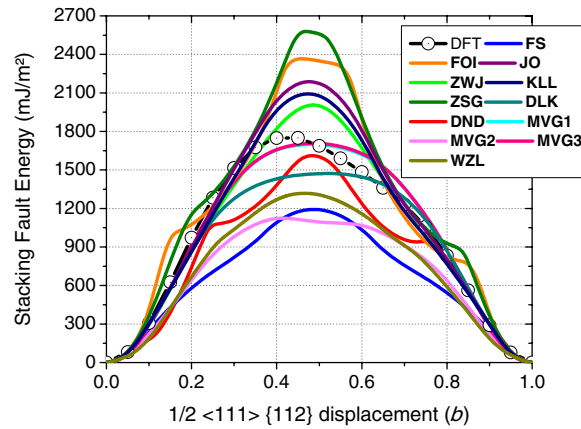

Figure 5. Comparison between DFT and the potentials of the $1/2\langle 1\,1\,1\rangle\{1\,1\,2\}$ stacking fault energy profile.

trend with respect to the order by which the interface energy depends on interface orientation is adequately predicted only by MVG1, DND, FOI and ZWJ. This agreement, however, does not imply that the structure of the GBs is also correctly predicted by these four potentials.

5.2. Line defects

Figure 7 presents the $1/2\langle 1\,1\,1\rangle$ atomic row displacement energy curves, also known as inter-row potential (IRP), calculated by both DFT and the interatomic potentials. The IRP provides information with respect to the SD core structure and can be used to model its movement (see, e.g., [94]). The DFT calculated IRP shows a wide plateau near the middle of the reaction path, which is only reproduced by MVG2. While the curves for FOI, ZSG and DND exhibit unphysical humps, the other curves show smooth behaviour with a well-defined
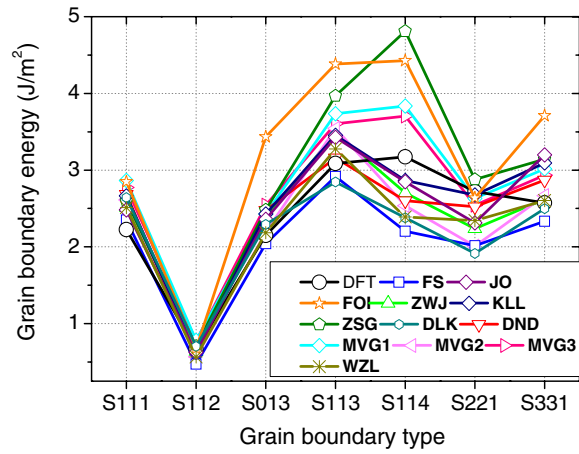
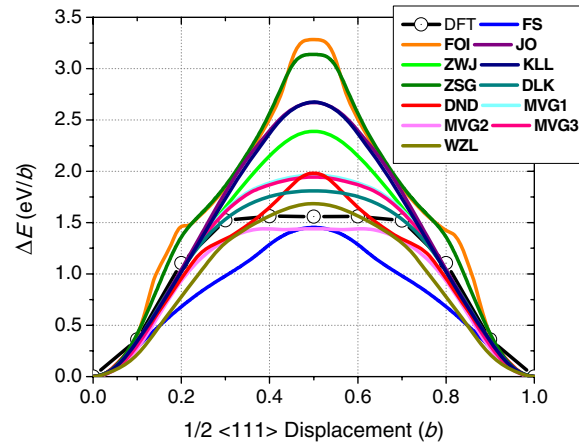**Figure 6.** GB interface energy per unit area for various grain boundary configurations.

Figure 7. Comparison between DFT and the potentials for the energy difference during a ⟨1 1 1⟩ atomic row displacement.

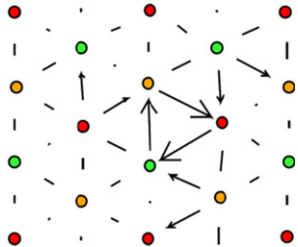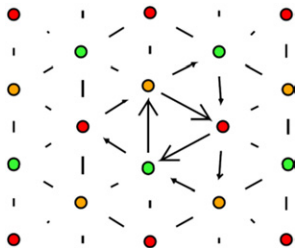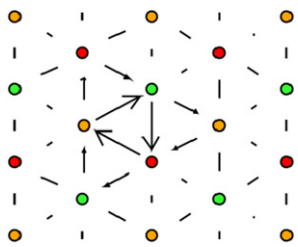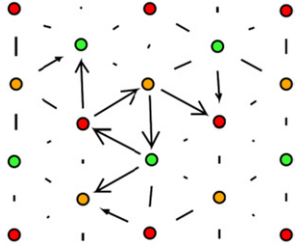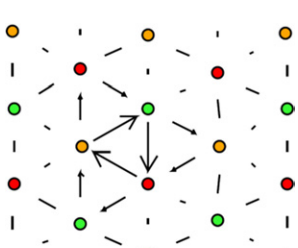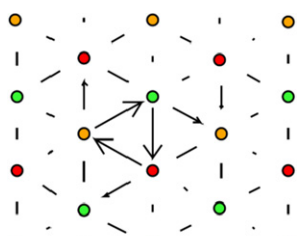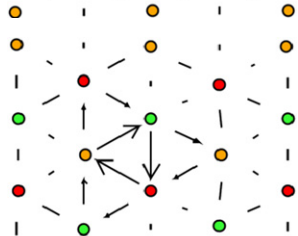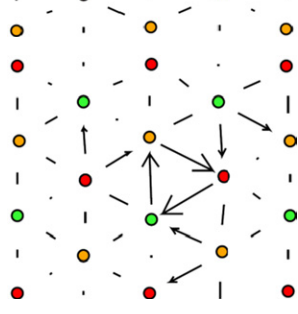single maximum. From all the smooth curves, only FS, MVG2 and WZL provide results within 10% of the DFT data.

In table 5 we present the SD core structure, movement mechanism under the ⟨1 1 1⟩{1 1 0} shear load and the corresponding Peierls stress, calculated using the potentials. The Peierls stress for a 1/2⟨1 1 1⟩{1 1 0} ED is also presented in table 5. The dislocation core structure is visualized by means of differential displacement maps [51]. For all bcc transition metals, and W in particular, DFT predicts a compact isotropic core structure for a 1/2⟨1 1 1⟩ SD [64–66, 91, 95–98]. Consistent with DFT results, the compact core is reproduced by ZSG, DLK, MVG (all), FOI and ZWJ. The three fold core structure is predicted by FS, JO, KLL, DND and WZL. Note that FOI and ZSG fail to reproduce (even qualitatively) the DFT-predicted γ-lines and IRP profile, but adequately describe the SD core structure. Hence, there is no direct correlation between the shape of the IRP profile and SD core structure, although such correlation has been speculated in the literature [99]. We note that similar calculations for FS, ZWJ and MVG3 were performed in [100]. Except for ZWJ, which was found to exhibit a degenerate core in [100], our results are in agreement with [100].

Table 5. SD core structure, SD glide path and Peierls stress for ED and SD. The SD and ED were generated and loaded in crystals so that the maximum resolved shear stress (MRSS) was exerted in a {1 1 0} plane. EDs were always seen to glide in the MRSS plane, i.e., {1 1 0} plane.

Method	Core structure	Mechanism of SD movement	τ_P screw	τ_P edge
DFT		Glide in {1 1 0} [66]	1.71 GPa [66]	
FS		Split & glide in {1 1 0}	3.98 GPa	38 MPa
JO		Split & glide in {1 1 2}	4.4 GPa	85 MPa
FOI		Transformation into degenerate core and glide of 1/6 ⟨1 1 1⟩ partial in {1 1 2} with formation of fault	15 GPa	6 GPa
ZWJ		Glide in {1 1 2}	4.1 GPa	50 MPa

Table 5. (Continued.)

Method	Core structure	Mechanism of SD movement	τ_P screw	τ_P edge
KLL		Split & glide in {1 1 2}	4.2 GPa	85 MPa
ZSG		Transformation into degenerate core and glide of 1/6 ⟨1 1 1⟩ partial in {1 1 2} with formation of fault	8.2 GPa	4.2 GPa
DLK		Glide in {1 1 2}	2.9 GPa	10 MPa
DND		Transformation into degenerate core and glide of 1/6 ⟨1 1 1⟩ partial in {1 1 2} with formation of fault	5.5 GPa	1.4 GPa
MVG1		Glide in {1 1 2}	3.55 GPa	1 MPa

MVG2		Glide in {1 1 0}	0.98 GPa	3 MPa
MVG3		Glide in inclined {1 1 0}	4.43 GPa	3 MPa
WZL		Split & glide in {1 1 2}	1.9 GPa	180 MPa

The mechanism of dislocation movement under $\langle 1\,1\,1 \rangle \{1\,1\,0\}$ shear load was also found to essentially depend on the applied potential. Overall, it is possible to distinguish three frequently observed mechanisms, namely: (i) glide of the compact core; (ii) split of the core into a planar structure and glide of the two dissociated dislocations; (iii) transformation of the core into a three fold degenerate structure and the emission of a gliding $1/6\langle 1\,1\,1 \rangle \{1\,1\,2\}$ partial dislocation (gliding in a $\{1\,1\,2\}$ plane) with the formation of a planar fault. We remind that according to DFT, the dislocation overcomes the Peierls barrier without changing its compact structure [66]. Among the tested potentials, qualitatively, the movement mechanism was predicted correctly by ZWJ and MVG (all), but the expected $\{1\,1\,0\}$ glide plane is reproduced only by the MVG2 and MVG3 potentials. The latter two potentials predict the Peierls stress to be 0.98 and 4.43 GPa, which bound the DFT value of 1.7 GPa [66]. The values of the Peierls stress of the SD obtained with other potentials are not discussed as the movement mechanism is inconsistent with the DFT predictions. We note that for FS, ZWJ and MVG3 similar calculations were performed in [100]. While the same Peierls stress is obtained for ZWJ, the values reported in [100], i.e., 2.0 and 1.8 GPa for FS and MVG3, respectively, are about a factor two lower than the ones reported in table 5. The discrepancy might be related to the calculation method, from which the Peierls stress was obtained. In [100], the Peierls stress is derived from the energy barrier obtained using a nudged elastic band method (NEB) relaxation-activation method [101] in a manner proposed by Gröger and Vitek [102]; while in this work the Peierls stress follows from static loading of a crystal (see section 2), applied in small increments to achieve the displacement of the core.

With respect to the ED, in all cases its core structure was found to be planar non-split, being very similar to that studied previously in bcc Fe [103, 104]. Three potentials (FOI, ZSG, DND)
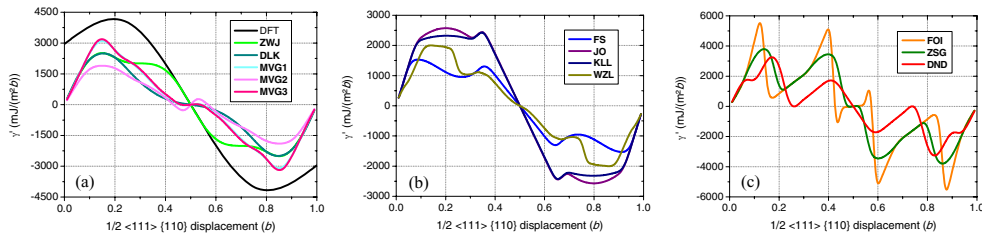
Figure 8. Derivative of the $1/2\langle 1\,1\,1\rangle\{1\,1\,0\}$ γ-line corresponding with DFT and potentials that exhibit, *a*) glide of the compact SD core, *b*) planar split and glide of the dissociated SD, and *c*) threefold degenerate split of the SD and glide of a partial.

have shown exceptional results: a split in the $\{1\,1\,0\}$ plane into two partials connected by a stacking fault. Note that exactly those three potentials were also found to predict an unphysical shape for the $\{1\,1\,0\}$ γ-line (see figure 4). As a result of the splitting, the dislocation moves by removal and generation of stacking faults in the $\{1\,1\,0\}$ glide plane, which requires a very high critical shear stress exceeding 1 GPa. All other potentials reveal a Peierls stress in the range of 1–180 MPa, which is consistent with the values obtained in bcc Fe using DFT-derived potentials [105]. Experimental data for the Peierls stress of EDs in bcc W is not available, to our knowledge.

Based on the results of this section, we conclude that the most appropriate potentials, i.e., describing properties of extended defects in line with DFT data (qualitatively or quantitatively), are MVG2 and MVG3.

To conclude this section, we attempt to correlate the γ-line (for $\{1\,1\,0\}$ planes, but the same holds for $\{1\,1\,2\}$ planes) corresponding to the different potentials with their observed dislocation behaviour. In figure 8 the derivative of the $\{1\,1\,0\}$ γ-lines from DFT and the potentials are summarized and classified into three categories. The derivative characterizes the force to be overcome by a dislocation in the $\{1\,1\,0\}$ plane. The first class (figure 8(*a*)) is consistent with DFT data, which predicts a single maximum and is consistent with the observed glide of the compact SD core (mechanism (i)). The second class (figure 8(*b*)) is characterized by a shallow maximum just beside the global maximum and is representative of the observed planar split and glide of a SD (mechanism (ii)). The third class exhibits two clearly distinct maxima of similar height and is representative of the observed transformation of a SD into a threefold degenerate core and glide of a partial (mechanism (iii)) or planar split and glide of an ED. Thus, figure 8 suggests a correlation between the stacking fault energy derivative and the path that the SD follows under shear of the crystal due to externally applied stress. The potentials predicting the barriers to be comparable to the DFT value result in stable SD glide in a $\{1\,1\,0\}$ or $\{1\,1\,2\}$ plane. However, the core of the SD apparently undergoes essential modification prior to the Peierls stress being reached in the case of the potentials grouped in figure 8(*b*). For that reason, the glide of the SD is realized along with the well-pronounced dislocation split. For the potentials grouped in figure 8(*c*), the resistance against shear is apparently so strong that the resolved shear stress is high enough to emit a partial dislocation in a $\{1\,1\,2\}$ plane, as we observed in the static simulations involving load. With these observations we conclude that adequate reproduction of the equilibrium core structure and γ-line curve is not enough to ensure a stable $\{1\,1\,0\}$ glide by the SD upon external load at 0 K. For instance, no clear reason was found for the difference in the SD glide plane for MVG1 and MVG3, given that they provide almost identical γ-lines and SD core structures. Apparently, competing mechanisms such as glide in an inclined $\{1\,1\,2\}$ plane or partial dislocation emission may come into play

Table 6. Schematic summary of the performance of the potentials for different physical properties.

Property	FS	JO	FOI	ZWJ	KLL	ZSG	DLK	DND	MVG1	MVG2	MVG3	WZL
Elastic constants	C	C	C	C	IC	C	C	C	C	C	C	C
E_f (Vac)	C	C	C	C	C	C	C	C	C	C	C	C
E_m (Vac)	UE	C	IC	C	C	IC	C	C	C	UE	C	UE
E_b (Di-Vac)	IC	IC	IC	IC	IC	IC	IC	UE	UE	IC	UE	UE
E_f (SIA)	UE[a]	IC	IC	IC	IC	IC	IC	C	C	C	C	C
$\langle 1\,1\,1 \rangle$ row potential	C	OE	IC	OE	OE	IC	OE	IC	OE	C	OE	C
Screw dislocation core	IC	IC	C	C	IC	C	C	IC	C	C	C	IC
Screw dislocation glide	IC	IC	IC	C	IC	IC	IC	IC	C	C	C	IC
Edge dislocation glide	C	C	IC	C	C	IC	C	IC	C	C	C	C
Free surface	UE	UE	UE	UE	UE	UE	UE	UE	UE	C	UE	UE
Grain boundary	UE	C	C	C	C	C	C	UE	C	UE	C	UE
Gamma surface cuts	UE	C	IC	C	C	IC	UE	IC	C	UE	C	UE
R_{cut}	2nn	2nn	2nn	2nn	2nn	2nn	6nn	2nn	5nn	4nn	5nn	2nn

IC–Inconsistent with experimental or DFT data.
C–Consistent with experimental or DFT data.
OE–Overestimation compared to experimental or DFT data.
UE–Underestimation compared to experimental or DFT data.
[a] Both AT and JW are consistent with the DFT data.

depending on the other properties of the potential, i.e., generalized stacking fault energy surface and polarizability of the SD core as a function of external load. As an indication as to what may be done towards further development of the potentials, we suggest verifying, or even including in the fitting, the core structure of the dislocation in the saddle point of the Peierls barrier, which could be obtained by *ab initio* calculations.

6. Summary

In this last section we summarize the performance of the tested potentials by identifying their strong and weak points. Table 6 presents a schematic summary of the potentials' performance, which is evaluated as 'consistent' (C) with experimental or DFT data if there is a qualitative (correct order or smooth curve) and quantitative (within 10% of the given range) agreement; 'inconsistent' (IC) if there is no qualitative agreement; 'underestimated' (UE) if there is qualitative agreement but the target value is underestimated by more than 10%; and 'overestimated' (OE) in the case of qualitative agreement but the target value is overestimated by more than 10%. Depending on the target application, a compromise between the performance and computational speed (R_{cut}) can be achieved by selecting an appropriate version of the potential. The results presented here can serve as an initial guide and reference list for both the modelling of atomically-driven phenomena in bcc tungsten, and the further development of its potentials.

Acknowledgments

References

[1] Zinkle S J 2005 *Phys. Plasmas* **12** 058101

[2] Rieth M *et al* 2011 *J. Nucl. Mater.* **417** 463

[3] Rieth M *et al* 2013 *J. Nucl. Mater.* **432** 482

[4] Gröger R, Bailey A G and Vitek V 2008 *Acta Mater.* **56** 5401

[5] Mrovec M, Elsässer C and Gumbsch P 2009 *Phil. Mag.* **89** 3179

[6] Srivastava K, Gröger R, Weygand D and Gumbsch P 2013 *Int. J. Plasticity* **47** 126

[7] Juslin N, Jansson V and Nordlund K 2010 *Phil. Mag.* **90** 3581

[8] Troev T, Nankov N and Yoshiie T 2011 *Nucl. Inst. Meth. Phys. Res. Sec.* B **269** 566

[9] Fu B, Xu B, Lai W, Yuan Y, Xu H, Li C, Jia Y and Liu W 2013 *J. Nucl. Mater.* **441** 24

[10] Sand A E, Dudarev S L and Nordlund K 2013 *Europhys. Lett.* **103** 46003

[11] Johnson R A and Wilson W D 1972 *Interatomic Potentials and Simulation of Latticde Defects* ed P C Gehlen *et al* (New York: Plenum) p 301
   This concerns the pair potential for tungsten.

[12] Johnson R A and White P J 1978 *Phys. Rev.* B **18** 2940

[13] Johnson R A 1983 *Phys. Rev.* B **27** 2014

[14] Mundim K C, Malbouisson L A C, Dorfman S, Fuks D, Van Humbeeck J and Liubich V 2001 *J. Mol. Struct. (Theochem)* **539** 191

[15] Finnis M W and Sinclair J E 1984 *Phil. Mag.* A **50** 45

[16] Ackland G J and Thetford R 1987 *Phil. Mag.* A **56** 15

[17] Johnson R A and Oh D J 1989 *J. Mater. Res.* **4** 1195

[18] Foiles S M 1993 *Phys. Rev.* B **48** 4287

[19] Wang Y R and Boercker D B 1995 *J. Appl. Phys.* **78** 122

[20] Zhou X W *et al* 2001 *Acta Mater.* **49** 2939

[21] Kong L T, Li X Y, Lai W S, Liu J B and Liu B X 2002 *Japan. J. Appl. Phys.* **41** 4503

[22] Gong H R, Kong L T, Lai W S and Liu B X 2003 *Phys. Rev.* B **68** 144201

[23] Zhang R F, Shen Y X, Gong H R, Kong L T and Liu B X 2004 *J. Phys. Soc. Japan* **73** 2023

[24] Zhang R F, Kong L T, Gong H R and Liu B X 2004 *J. Phys.: Condens. Matter* **16** 5251

[25] Zhang R F, Shen Y X, Yan H F and Liu B X 2005 *J. Phys. Chem.* B **109** 4391

[26] Dai X D, Li J H and Kong Y 2007 *Phys. Rev.* B **75** 052102

[27] Derlet P M, Nguyen-Manh D and Dudarev S L 2007 *Phys. Rev.* B **76** 054107

[28] Björkas C, Nordlund K and Dudarev S 2009 *Nucl. Instrum. Methods Phys. Res.* B **267** 3204
   Björkas C, Nordlund K and Dudarev S 2010 *Nucl. Instrum. Methods Phys. Res.* B **268** 1529 (erratum)

[29] Juslin N and Wirth B D 2013 *J. Nucl. Mater.* **432** 61

[30] Marinica M-C *et al* 2013 *J. Phys. Condens. Matter* **25** 395502

[31] Wang J, Zhou Y L, Li M and Hou Q 2014 *Modelling Simul. Mater. Sci. Eng.* **22** 015004

[32] Hu W, Shu W and Zhang B 2002 *Comput. Mater. Sci.* **23** 175

[33] Xie Q and Chen P 1997 *Phys. Rev.* B **56** 5235

[34] Henriksson K O E, Nordlund K, Keinonen J, Sundholm D and Patzschke M 2004 *Phys. Scr.* **T108** 95

[35] Juslin N, Erhart P, Träskelin P, Nord J, Enriksson K O, Nordlund K, Salonen E and Albe K 2005 *J. Appl. Phys.* **98** 123520

[36] Mrovec M, Gröger R, Bailey A G, Nguyen-Manh D, Elsässer C and Vitek V 2007 *Phys. Rev.* B **75** 104119

[37] Baskes M I 1992 *Phys. Rev.* B **46** 2727

[38] Lee B J, Baskes M I, Kim H and Choo Y K 2001 *Phys. Rev.* B **64** 184102

[39] Park H, Fellinger M R, Lenosky T J, Tripton W W, Trinkle D R, Rudin S P, Woodward C, Wilkins J W and Hennig R G 2012 *Phys. Rev.* B **85** 214121
[40] Carlsson A E 1991 *Phys. Rev.* B **44** 6590
[41] Xu W and Adams J B 1994 *Surf. Sci.* **301** 371
[42] Daw M S and Baskes M I 1984 *Phys. Rev.* B **29** 6443
[43] Ercolessi F 1983 Molecular dynamics studies of gold: bulk, defects, surfaces and clusters *PhD Thesis* University of Trieste
[44] Ercolessi F, Tosatti E and Parrinello M 1986 *Phys. Rev. Lett.* **57** 719
[45] Kresse G and Hafner J 1993 *Phys. Rev.* B **47** 558
[46] Kresse G and Furthmuller J 1996 *Phys. Rev.* B **54** 11169
[47] Blochl P E 1994 *Phys. Rev.* B **50** 17953
[48] Kresse G and Joubert D 1999 *Phys. Rev.* B **59** 1758
[49] Vosko S H, Wilk L and Nusair M 1980 *Can. J. Phys.* **58** 1200
[50] Perdew J P, Chevary J A, Vosko S H, Jackson K A, Pederson M R, Singh D J and Fiolhais C 1992 *Phys. Rev.* B **46** 6671
[51] Vitek V, Perrin R C and Bowen D K 1970 *Phil. Mag.* **21** 1049
[52] Osetsky Yu N and Bacon D J 2003 *Modelling Simul. Mater. Sci. Eng.* **11** 427
[53] Rodney D 2004 *Acta Mater.* **52** 607
[54] Kittel C 1976 *Introduction to Solid State Physics* 5th edn (Wiley: New York)
[55] Brandes E A and Brook G B 1992 *Smithells Metals Reference Book* 7th edn (Oxford: Butterworth-Heinemann)
[56] Simmons G and Wang H 1971 *Single Crystal Elastic Constants and Calculated Aggregate Properties: A Handbook* 2nd edn (Cambridge, MA: M.I.T. Presss)
[57] Kittel C 1971 *Introduction to Solid State Physics* 4th edn (New York: Wiley)
[58] Maier K, Peo M, Saile B, Schaefer H E and Seeger A 1979 *Phil. Mag.* A **40** 701
[59] Tietze M, Takaki S, Schwirtlich I A and Schultz H 1982 *Point Defects and Defect Interactions in Metals* ed J-I Takamura *et al* (Amsterdam: North Holland) p 266
[60] Ziegler R and Schaefer H E 1987 *Vacancies and Interstititals in Metals and Alloys* ed C Abromeit and H Wollenberger (Switzerland: Trans Tech) p 145
[61] Ziegler J F, Biersack J P and Littmark U 1985 *The Stopping and Range of Ions in Matter* (New York: Pergamon)
[62] Ercolessi F and Adams J B 1994 *Europhys. Lett.* **26** 583
[63] Mendelev M I, Han S, Srolovitz D J, Ackland G J, Sun D Y and Asta M 2003 *Phil. Mag.* **83** 3977
[64] Romaner L, Ambrosch-Drax C and Pippan R 2010 *Phys. Rev. Lett.* **104** 195503
[65] Li H, Wurster S, Motz C, Romaner L, Ambrosch-Draxl C and Pippan R 2012 *Acta Mater.* **60** 748
[66] Samolyuk G D, Osetsky Y N and Stoller R E 2013 *J. Phys. Condens. Matter* **25** 025403
[67] Ventelon L, Willaime F, Fu C-C, Heran M and Ginoux I 2012 *J. Nucl. Mater.* **425** 16
[68] Lassner E and Schubert W D 1999 *Tungsten: Properties, Chemistry, Technology of the Element, Alloys, and Chemical Compounds* (New York: Kluwer Academic)
[69] Lide D R 2004 *Handbook of Chemistry and Physics* 85th edn (Boca Raton, FL: CRC Press)
[70] Gray D E 1957 *American Institute of Physics Handbook* (New York: McGraw-Hill)
[71] Ehrhart P and Ullmaier H 1991 *Atomic Defects in Metals (Landolt-Börnstein New Series, Group III* vol 25) (Springer-Verlag, Berlin)
[72] Heinola K and Ahlgren T 2010 *J. Appl. Phys.* **107** 113531
[73] Ochs T, Beck O, Elsasser C and Meyer B 2000 *Phil. Mag.* A **80** 351
[74] Skriver H L 1985 *Phys. Rev.* B **31** 1909
[75] Bujard P 1982 *Thesis dissertation* University of Geneva
[76] Featherstone F H and Neighbours J R 1963 *Phys. Rev.* **130** 1324
[77] Ayres R A, Shanette G and Stein D 1975 *J. Appl. Phys.* **46** 1526
[78] Bolef D I and Klerk J D 1962 *J. Appl. Phys.* **33** 2311
[79] Muzyk M, Nguyen-Manh D, Kurzydłowski K J, Baluc N L and Dudarev S L 2011 *Phys. Rev.* B **84** 104115
[80] Nguyen-Manh D, Horsfield A P and Dudarev S L 2006 *Phys. Rev.* B **73** 020101

[81]   Becquart C S and Domain C 2007 *Nucl. Instrum. Methods Phys. Res.* B **255** 23
[82]   Górecki T 1974 *Z. Metallk.* **65** 426
[83]   Rasch K-D, Siegel R W and Schultz H 1980 *Phil. Mag.* A **41** 91
[84]   Smedskjaer L C, Chason M K and Siegel R W 1983 *Bull. Am. Phys. Soc.* **28** 242
[85]   Heinola K, Ahlgren T, Nordlund K and Keinonen J 2010 *Phys. Rev.* B **82** 094102
[86]   Park J Y, Huang H C W, Siegel R W and Balluffi R W 1983 *Phil. Mag.* A **48** 397
[87]   Kato D, Iwakiri H and Morishita K 2011 *J. Nucl. Mater.* **417** 1115
[88]   Vitos L, Ruban A V, Skriver H L and Kollár J 1998 *Surf. Sci.* **411** 186
[89]   Tyson W R and Miller W A 1977 *Surf. Sci.* **62** 267
[90]   de Boer F R, Boom R, Mattens W C M, Miedema A R and Niessen A K 1988 *Cohesion in Metals*
         (Amsterdam: North-Holland)
[91]   Frederiksen S L and Jacobsen K W 2003 *Phil. Mag.* **83** 365
[92]   Peierls R E 1940 *Proc. Phys. Soc.* **52** 34
[93]   Nabarro F R N 1947 *Proc. Phys. Soc.* **59** 256
[94]   Chen Z, Kioussis N, Ghoniem N and Hasebe T 2008 *Phys. Rev.* B **77** 014103
[95]   Ismail-Beigi S and Arias T A 2000 *Phys. Rev. Lett.* **84** 1499
[96]   Ventelon L and Willaime F 2007 *J. Comput. Aided Mater. Des.* **14** (suppl. 1) 85
[97]   Kaburaki H, Shimizu F, Ogata S, Yamaguchi M, Kano T, Kimizuka H and Itakura M 2007 Annual
         Report on Earth Simulator Center
[98]   Shimizu F, Ogata S, Kano T, Li J and Kaburaki H 2007 *J. Earth Simulator* **7** 17
[99]   Chiesa S, Gilbert M R, Dudarev S L, Derlet P M and Van Swygenhoven H 2009 *Phil. Mag.* **89** 3235
[100] Cereceda D, Stukowski A, Gilbert M R, Queyreau S, Ventelon L, Marinica M-C, Perlado J M and
         Marian J 2013 *J. Phys. Condens. Matter* **25** 085702
[101] Henkelman G, Johannesson G and Jonsson H 2000 *Progress on Theoretical Chemistry and Physics*
         (Dordrecht: Kluwer) p 269
[102] Gröger R and Vitek V 2012 *Modelling Simul. Mater. Sci. Eng.* **20** 035019
[103] Chen L, Wang C and Yu T 2006 *Comput. Mater. Sci.* **38** 39
[104] Monnet G and Terentyev D 2009 *Acta Mater.* **57** 1416
[105] Malerba L *et al* 2010 *J. Nucl. Mater.* **406** 19